Nuclear Physics B407 (1993) 515–535
North-Holland

NUCLEAR
PHYSICS B

Measurement of the proton structure function $F_2(x, Q^2)$ in the low-x region at HERA

H1 Collaboration

I. Abt[g], T. Ahmed[c], V. Andreev[x], B. Andrieu[aa], R.-D. Appuhn[k], M. Arpagaus[ah], A. Babaev[y], H. Bärwolff[ag], J. Bán[q], P. Baranov[x], E. Barrelet[ab], W. Bartel[k], U. Bassler[ab], H.P. Beck[ai], H.-J. Behrend[k], A. Belousov[x], Ch. Berger[a], H. Bergstein[a], G. Bernardi[ab], R. Bernet[ah], G. Bertrand-Coremans[d], M. Besançon[i], P. Biddulph[v], E. Binder[k], A. Bischoff[ag], J.C. Bizot[z], V. Blobel[m], K. Borras[h], P.C. Bosetti[b], V. Boudry[aa], C. Bourdarios[z], F. Brasse[k], U. Braun[b], W. Braunschweig[a], V. Brisson[z], D. Bruncko[q], L. Büngener[m], J. Bürger[k], F.W. Büsser[m], A. Buniatian[k,ak], S. Burke[s], G. Buschhorn[y], A.J. Campbell[k], T. Carli[y], F. Charles[ab], D. Clarke[e], A.B. Clegg[r], M. Colombo[h], J.A. Coughlan[e], A. Courau[z], Ch. Coutures[i], G. Cozzika[i], L. Criegee[k], J. Cvach[aa], S. Dagoret[ab], J.B. Dainton[s], M. Danilov[w], A.W.E. Dann[v], W.D. Dau[p], M. David[i], E. Deffur[k], B. Delcourt[z], L. Del Buono[ab], M. Devel[z], A. De Roeck[k], P. Dingus[aa], C. Dollfus[ai], J.D. Dowell[c], H.B. Dreis[b], A. Drescher[h], J. Duboc[ab], D. Düllmann[m], O. Dünger[m], H. Duhm[ℓ], R. Ebbinghaus[h], M. Eberle[ℓ], J. Ebert[af], T.R. Ebert[s], G. Eckerlin[k], V. Efremenko[w], S. Egli[ai], S. Eichenberger[ai], R. Eichler[ah], F. Eisele[n], E. Eisenhandler[t], N.N. Ellis[c], R.J. Ellison[v], E. Elsen[k], M. Erdmann[n], E. Evrard[d], L. Favart[d], A. Fedotov[w], D. Feeken[m], R. Felst[k], J. Feltesse[i], I.F. Fensome[c], J. Ferencei[k], F. Ferrarotto[ae], K. Flamm[k], W. Flauger[k,l], M. Fleischer[k], G. Flügge[b], A. Fomenko[x], B. Fominykh[w], M. Forbush[g], J. Formánek[ad], J.M. Foster[v], G. Franke[k], E. Fretwurst[ℓ], P. Fuhrmann[a], E. Gabathuler[s], K. Gamerdinger[y], J. Garvey[c], J. Gayler[k], A. Gellrich[m], M. Gennis[k], H. Genzel[a], R. Gerhards[k], L. Godfrey[g], U. Goerlach[k], L. Goerlich[f], M. Goldberg[ab], A.M. Goodall[s], I. Gorelov[w], P. Goritchev[w], C. Grab[ah], H. Grässler[b], R. Grässler[b], T. Greenshaw[s], H. Greif[y], G. Grindhammer[y], C. Gruber[p], J. Haack[ag], D. Haidt[k], L. Hajduk[f], O. Hamon[ab], D. Handschuh[k], E.M. Hanlon[r], M. Hapke[k], J. Harjes[k], R. Haydar[z], W.J. Haynes[e], J. Heatherington[t], V. Hedberg[u], G. Heinzelmann[m], R.C.W. Henderson[r], H. Henschel[ag], R. Herma[a], I. Herynek[ac], W. Hildesheim[ab], P. Hill[k], C.D. Hilton[v], J. Hladký[ac], K.C. Hoeger[v], Ph. Huet[d], H. Hufnagel[n], N. Huot[ab], M. Ibbotson[v], H. Itterbeck[a], M.-A. Jabiol[i], A. Jacholkowska[z], C. Jacobsson[u], M. Jaffre[z], T. Jansen[k], L. Jönsson[u], K. Johannsen[m], D.P. Johnson[d],

L. Johnson[r], H. Jung[b], P.I.P. Kalmus[t], S. Kasarian[k], R. Kaschowitz[b], P. Kasselmann[ℓ], U. Kathage[p], H. H.Kaufmann[ag], I.R. Kenyon[c], S. Kermiche[z], C. Keuker[a], C. Kiesling[y], M. Klein[ag], C. Kleinwort[m], G. Knies[k], W. Ko[g], T. Köhler[a], H. Kolanoski[h], F. Kole[g], S.D. Kolya[v], V. Korbel[k], M. Korn[h], P. Kostka[ag], S.K. Kotelnikov[x], M.W. Krasny[f,ab], H. Krehbiel[k], D. Krücker[b], U. Krüger[k], J.P. Kubenka[y], H. Küster[b], M. Kuhlen[y], T. Kurča[q], J. Kurzhöfer[h], B. Kuznik[af], F. Lamarche[aa], R. Lander[g], M.P.J. Landon[t], W. Lange[ag], R. Langkau[ℓ], P. Lanius[y], J.F. Laporte[i], A. Lebedev[x], A. Leuschner[k], C. Leverenz[k], S. Levonian[k,x], D. Lewin[k], Ch. Ley[b], A. Lindner[h], G. Lindström[ℓ], F. Linsel[k], J. Lipinski[m], P. Loch[k], H. Lohmander[u], G.C. Lopez[t], D. Lüers[y,l], N. Magnussen[af], E. Malinovski[x], S. Mani[g], P. Marage[d], J. Marks[j], R. Marshall[v], J. Martens[af], R. Martin[s], H.-U. Martyn[a], J. Martyniak[f], S. Masson[b], A. Mavroidis[t], S.J. Maxfield[s], S.J. McMahon[s], A. Mehta[v], K. Meier[o], D. Mercer[v], T. Merz[k], C.A. Meyer[ai], H. Meyer[af], J. Meyer[k], S. Mikocki[f,z], V. Milone[ae], E. Monnier[ab], F. Moreau[aa], J. Moreels[d], J.V. Morris[e], K. Müller[ai], P. Murín[q], S.A. Murray[v], V. Nagovizin[w], B. Naroska[m], Th. Naumann[ag], D. Newton[r], D. Neyret[ab], H.K. Nguyen[ab], F. Niebergall[m], R. Nisius[a], G. Nowak[f], G.W. Noyes[c], M. Nyberg[u], H. Oberlack[y], U. Obrock[h], J.E. Olsson[k], S. Orenstein[aa], F. Ould-Saada[m], C. Pascaud[z], G.D. Patel[s], E. Peppel[k], S. Peters[y], H.T. Phillips[c], J.P. Phillips[v], Ch. Pichler[ℓ], W. Pilgram[b], D. Pitzl[ah], S. Prell[k], R. Prosi[k], G. Rädel[k], F. Raupach[a], K. Rauschnabel[h], P. Reimer[ac], S. Reinshagen[k], P. Ribarics[y], V. Riech[ℓ], J. Riedlberger[ah], S. Riess[m], M. Rietz[b], S.M. Robertson[c], P. Robmann[ai], R. Roosen[d], A. Rostovtsev[w], C. Royon[i], M. Rudowicz[y], M. Ruffer[ℓ], S. Rusakov[x], K. Rybicki[f], N. Sahlmann[b], E. Sanchez[y], D.P.C. Sankey[e], M. Savitsky[k], P. Schacht[y], P. Schleper[n], W. von Schlippe[t], C. Schmidt[k], D. Schmidt[af], W. Schmitz[b], V. Schröder[k], M. Schulz[k], B. Schwab[n], A. Schwind[ag], W. Scobel[ℓ], U. Seehausen[m], R. Sell[k], A. Semenov[w], V. Shekelyan[w], I. Sheviakov[x], H. Shooshtari[y], L.N. Shtarkov[x], G. Siegmon[p], U. Siewert[p], Y. Sirois[aa], I.O. Skillicorn[j], P. Smirnov[x], J.R. Smith[g], L. Smolik[k], Y. Soloviev[x], H. Spitzer[m], P. Staroba[ac], M. Steenbock[m], P. Steffen[k], R. Steinberg[b], B. Stella[ae], K. Stephens[v], J. Stier[k], U. Stösslein[ag], J. Strachota[k], U. Straumann[ai], W. Struczinski[b], J.P. Sutton[c], R.E. Taylor[aj,z], V. Tchernyshov[w], C. Thiebaux[aa], G. Thompson[t], I. Tichomirov[w], P. Truöl[ai], J. Turnau[f], J. Tutas[n], L. Urban[y], A. Usik[x], S. Valkar[ad], A. Valkarova[ad], C. Vallée[ab], P. Van Esch[d], A. Vartapetian[k,ak], Y. Vazdik[x], M. Vecko[ac], P. Verrecchia[i], R. Vick[m], G. Villet[i], E. Vogel[a], K. Wacker[h], I.W. Walker[r], A. Walther[h], G. Weber[m], D. Wegener[h], A. Wegner[k], H.P Wellisch[y], S. Willard[g], M. Winde[ag], G.-G. Winter[k], Th. Wolff[ah], L.A. Womersley[s], A.E. Wright[v], N. Wulff[k], T.P. Yiou[ab], J. Žáček[ad], P. Závada[ac], C. Zeitnitz[ℓ], H. Ziaeepour[z], M. Zimmer[k], W. Zimmermann[k] and F. Zomer[z]

[a] *I. Physikalisches Institut der RWTH, Aachen, Germany*[2]
[b] *III. Physikalisches Institut der RWTH, Aachen, Germany*[2]
[c] *School of Physics and Space Research, University of Birmingham, Birmingham, UK*[3]
[d] *Inter-University Institute for High Energies ULB-VUB, Brussels, Belgium*[4]
[e] *Rutherford Appleton Laboratory, Chilton, Didcot, UK*[3]
[f] *Institute for Nuclear Physics, Cracow, Poland*[5]
[g] *Physics Department and IIRPA, University of California, Davis, CA, USA*[6]
[h] *Institut für Physik, Universität Dortmund, Dortmund, Germany*[2]
[i] *DAPNIA, Centre d'Etudes de Saclay, Gif-sur-Yvette, France*
[j] *Department of Physics and Astronomy, University of Glasgow, Glasgow, UK*[3]
[k] *DESY, Hamburg, Germany*[2]
[ℓ] *I. Institut für Experimentalphysik, Universität Hamburg, Hamburg, Germany*[2]
[m] *II. Institut für Experimentalphysik, Universität Hamburg, Hamburg, Germany*[2]
[n] *Physikalisches Institut, Universität Heidelberg, Heidelberg, Germany*[2]
[o] *Institut für Hochenergiephysik, Universität Heidelberg, Heidelberg, Germany*[2]
[p] *Institut für Reine und Angewandte Kernphysik, Universität Kiel, Kiel, Germany*[2]
[q] *Institute of Experimental Physics, Slovak Academy of Sciences, Košice, Slovak Republic*
[r] *School of Physics and Materials, University of Lancaster, Lancaster, UK*[3]
[s] *Department of Physics, University of Liverpool, Liverpool, UK*[3]
[t] *Queen Mary and Westfield College, London, UK*[3]
[u] *Physics Department, University of Lund, Lund, Sweden*[7]
[v] *Physics Department, University of Manchester, Manchester, UK*[3]
[w] *Institute for Theoretical and Experimental Physics, Moscow, Russian Federation*
[x] *Lebedev Physical Institute, Moscow, Russian Federation*
[y] *Max-Planck-Institut für Physik, Munich, Germany*[2]
[z] *LAL, Université de Paris-Sud, IN2P3-CNRS, Orsay, France*
[aa] *LPNHE, Ecole Polytechnique, IN2P3-CNRS, Palaiseau, France*
[ab] *LPNHE, Universités Paris VI and VII, IN2P3-CNRS, Paris, France*
[ac] *Institute of Physics, Czech Academy of Sciences, Praha, Czech Republic*
[ad] *Nuclear Center, Charles University, Praha, Czech Republic*
[ae] *INFN Roma and Dipartimento di Fisica, Universita "La Sapienza", Rome, Italy*
[af] *Fachbereich Physik, Bergische Universität Gesamthochschule Wuppertal, Wuppertal, Germany*[2]
[ag] *DESY, Institut für Hochenergiephysik, Zeuthen, Germany*[2]
[ah] *Institut für Mittelenergiephysik, ETH, Zürich, Switzerland*[8]
[ai] *Physik-Institut der Universität Zürich, Zürich, Switzerland*[8]
[aj] *Stanford Linear Accelerator Center, Stanford, CA, USA*
[ak] *Yerevan Physical Institute, Yerevan, Armenia*

Received 30 August 1993
Accepted for publication 3 September 1993

A measurement of the proton structure function $F_2(x, Q^2)$ is presented with about 1000 neutral current deep inelastic scattering events for Bjorken x in the range $x \simeq 10^{-2} - 10^{-4}$ and $Q^2 > 5\,\mathrm{GeV}^2$. The measurement is based on an integrated luminosity of 22.5 nb^{-1} recorded by the H1 detector in the first year of HERA operation. The structure function $F_2(x, Q^2)$ shows a significant rise with decreasing x.

1. Introduction

Deep inelastic lepton–nucleon scattering experiments have provided a remarkable insight into the structure of matter at small distances. The discovery of the partonic structure of nucleons in the late sixties [1] and the subsequent observation of violation of Bjorken scaling laid solid foundations for Quantum Chromodynamics, the theory of strong interactions of quarks and gluons. At the electron–proton collider HERA, in which 26.7 GeV electrons collide with 820 GeV protons, deep inelastic scattering off proton constituents carrying a very small fraction x of the proton momentum can be studied. Furthermore the proton structure will be probed at 10 times smaller distances than previously accessible.

In this paper we present a measurement of the proton structure function $F_2(x, Q^2)$ at low x obtained from the analysis of neutral current deep inelastic scattering data collected with the H1 detector [2] in 1992, the first year of data taking at HERA. The data correspond to an integrated luminosity of 22.5 nb^{-1}. Preliminary results on F_2 from the H1 collaboration have been presented earlier [3]. Recently, the ZEUS collaboration has presented an F_2 measurement [4]. Our first measurement of neutral current cross sections based on a luminosity of 1.3 nb^{-1} was published in ref. [5].

The kinematics of the inclusive deep inelastic scattering process $\text{ep} \rightarrow \text{e}X$ at fixed centre-of-mass energy, $\sqrt{s}$, is determined by two independent Lorentz-invariant variables, conventionally chosen to be two of Bjorken x, momentum transfer Q^2 and y. The H1 experiment at HERA measures both the scattered electron and the hadronic final state, thus the collision kinematics can be determined from electron variables, hadron variables or a mixture of both. This novel feature of HERA experiments, compared to those operated in the fixed-target mode, allows a more precise measurement and provides an important cross-check of systematic effects. In addition, the cross section measurements using electron or hadron variables have a different sensitivity to the processes of real photon emission from the incoming and scattered electron. This allows to control experimentally the size of the radiative corrections. In the analysis presented in this paper the scaling variable y is determined in two ways. The first method uses the energy, E'_e, and the polar angle, θ_e, of the scattered electron

[1] Deceased.

[2] Supported by the Bundesministerium für Forschung und Technologie, Germany under contract numbers 6AC17P, 6AC47P, 6DO57I, 6HH17P, 6HH27I, 6HD17I, 6HD27I, 6KI17P, 6MP17I, and 6WT87P.

[3] Supported by the UK Science and Engineering Research Council.

[4] Supported by IISN-IIKW, NATO CRG-890478.

[5] Supported by the Polish State Committee for Scientific Research, grant 204209101.

[6] Supported in part by USDOE grant DE F603 91ER40674.

[7] Supported by the Swedish Natural Science Research Council.

[8] Supported by the Swiss National Science Foundation.

measured relative to the proton beam direction,

$$y_e = 1 - (E'_e/E_e)\sin^2(\theta_e/2), \tag{1}$$

where E_e is the energy of the incident electron. The second method determines y from the hadrons using the relation [6]

$$y_h = \sum_{\text{hadrons}} \frac{E_h - p_{z,h}}{2E_e}, \tag{2}$$

where E_h is the energy of a hadron and $p_{z,h}$ its momentum component along the incident proton direction. For an ideal 4π hermetic detector and, in the absence of real photon radiation by the incoming and scattered electron, the two y measurements are equivalent. The kinematical variable Q^2 is determined from the electron variables θ_e and E'_e as

$$Q_e^2 = 4E_eE'_e\cos^2(\theta_e/2), \tag{3}$$

and x is determined either from the electron variables

$$x_e = Q_e^2/(sy_e), \tag{4}$$

or, by using a mixture of the hadron measurement of y and the electron measurement of Q^2

$$x_m = Q_e^2/(sy_h). \tag{5}$$

The centre-of-mass energy squared s is given by $s = 4E_eE_p$, where E_p is the incident proton energy.

The Q^2 resolution is dominated by the electron energy resolution and is better than 10% in our acceptance region. The y_e resolution is better than 10% at large y_e ($y_e \simeq 0.5$) but deteriorates rapidly ($\delta y_e/y_e \sim 1/y_e$) at low y_e. The y_h resolution, on the contrary, is better than 20% at low y_h ($y_h \simeq 0.02$) but is worse than the y_e resolution for $y_h > 0.3$. Therefore it is advantageous to use the y_e measurement at large y and the y_h measurement at low y.

At HERA, where $s = 87\,600\,\text{GeV}^2$, for the first time values of $x = Q^2/ys$ in the range $x \simeq 10^{-2} - 10^{-4}$ can be measured in the deep inelastic regime ($Q^2 > 5\,\text{GeV}^2$). The x shape and Q^2 dependence of F_2 in this x range cannot be reliably predicted by extrapolating present fixed-target data. Available parametrizations for the low-x region rely on model assumptions such as a "Regge-type behaviour" of the parton distributions corresponding to a flat F_2 at small x, or alternatively, a "Lipatov behaviour" [7] corresponding to a strong rise of F_2 at small x. If $F_2(x, Q^2)$ grows sufficiently fast at low x, HERA will allow to test QCD in the domain of high parton densities and small $\alpha_s(Q^2) \ll 1$ coupling, where the standard linear QCD evolution equations are expected to fail, leading eventually to a breakdown of the parton picture [8].

The measurement of F_2 at low x is finally an important ingredient for the interpretation of hard collisions at future hadron colliders both for pp and heavy-ion collisions.

2. The H1 detector

A detailed description of the H1 detector and its performance can be found in ref. [2]. Below we shall discuss only those aspects which are relevant for the structure function measurement.

In this analysis we restrict ourselves to the low-x domain and $5\,\mathrm{GeV}^2 < Q^2 < 80\,\mathrm{GeV}^2$; the measurement of F_2 in the high-Q^2 region will be reported in a future publication. In the Q^2 region considered the scattered electrons are detected in the backward electromagnetic calorimeter (BEMC). The BEMC is made of 88 lead/scintillator sandwich stacks, each with a depth of 22 radiation lengths, corresponding to about one interaction length. The quadratic stacks, covering the angular range of $160° < \theta_e < 172.5°$, have a transverse dimension of 16 by 16 cm^2. Two pairs of 8 cm wavelength shifter bars cover opposite sides of these stacks. A 1.5 cm space resolution for the reconstructed centre-of-gravity of an electromagnetic cluster is achieved owing to an independent photodiode readout of each wavelength shifter. The systematic uncertainty on F_2 strongly depends on the absolute calibration of this detector, and on the knowledge of its resolution. The relative calibration of the BEMC stacks and the energy-dependent terms of its resolution are determined from test beam measurements. The absolute energy scale and the constant term of the BEMC resolution are determined using deep inelastic scattering events exploiting the redundancy in the measurement of the kinematical variables. The measured electron energy in the BEMC is compared with the one determined from the angle of the hadronic system and the electron angle. From these studies we conclude that the energy scale of the BEMC is known to 2% and its resolution is described by

$$\sigma(E'_e)/E'_e = 0.1/\sqrt{E'_e} \oplus 0.42/E'_e \oplus 0.03\,,$$

where E'_e is in GeV.

Charged-particle tracks are measured in two concentric jet-drift chamber modules (CJC) of angular acceptance 15°–165°. A superconducting coil provides a uniform magnetic field of 1.15 T in the tracking region which allows the determination of charged-particle momenta. Due to the limited angular acceptance of these chambers the majority of electrons scattered with $Q^2 < 80\,\mathrm{GeV}^2$ leave no track in the CJC. The polar angle θ_e is calculated from the position of the reconstructed event vertex and a reconstructed space point in the backward proportional chamber (BPC). The BPC has four wire planes and an angular acceptance of 155.5°–174.5°. The vertex position is determined on an event by event basis, from at least one track reconstructed in the CJC, originating from the interaction region. The accuracy of the polar-angle measurement has been derived from studies of a subsample of events in which the electron track has been reconstructed in the CJC and is found to be better than 5 mrad.

The hadron energies are measured in the highly segmented liquid argon calor-

imeter (LAr) [9], the BEMC and the instrumented iron backing calorimeter. The LAr calorimeter consists of an electromagnetic section with lead absorber and a hadronic section with stainless-steel absorber. The total depth of the electromagnetic part varies between 20 and 30 radiation lengths whereas the total depth of both calorimeters varies between 4.5 and 8 interaction lengths. The LAr calorimeter covers the angular range between 4° and 153°. The calibration of the LAr calorimeter segments has been obtained from test-beam measurements using electrons and pions [2,9,10]. The electromagnetic energy scale is verified to a 3% accuracy in the H1 detector by comparing the measured track momentum of electrons and positrons with the corresponding energy deposition in the calorimetric cells. The absolute scale of the hadronic energy is presently known to 7% as determined from studies of the p_t balance for deep inelastic scattering events.

The determination of y_h according to eq. (2) uses a combination of calorimetric measurements and reconstructed charged tracks in the central region. Double counting of the energy is avoided by masking calorimetric cells behind a track in a cylinder of 15 (25) cm in the electromagnetic (hadronic) calorimeter. The contribution of tracks to the y_h measurement is about 40 %. This reduces the influence of energy-scale uncertainties and improves the y_h resolution.

Electrons and photons emitted at very small angles with respect to the incoming electron direction are measured in an electron- and a photon-tagging calorimeter. These detectors are located 33 and 103 m downstream of the interaction point and have angular acceptances below 5 mrad and 0.5 mrad, respectively. The electron and photon taggers are designed to detect the e–γ coincidences from the low-Q^2 elastic radiative collisions $e + p \rightarrow e + \gamma + p$, used to measure the luminosity. The photon and electron taggers further allow us to control the size of the radiative corrections and the size of the photoproduction background to deep inelastic scattering, as will be discussed below.

In 1992 HERA was operated with 10 electron and 10 proton bunches, separated by 96 ns. Nine bunches were colliding, one electron and one proton bunch—termed pilot bunches—had no collision partner. The interaction region extends along the beam line with a $\sigma_z \simeq 25$ cm as determined by the length of the proton bunch.

3. Event selection and background subtraction

3.1. SELECTION OF DEEP INELASTIC SCATTERING CANDIDATES

The events used in this analysis are triggered by requiring a local energy deposit, or cluster, of more than 4 GeV in the BEMC. This trigger is dominated by interactions of beam protons with residual gas and beam line elements upstream of the H1 detector. Most of these events are efficiently rejected at the trigger level

using a time of flight system (TOF) [2] consisting of two scintillator planes installed behind the BEMC. In total we have recorded $\sim 5 \times 10^5$ events which are dominated by beam induced background and photoproduction interactions. A clean sample of deep inelastic scattering candidates is selected offline by the following requirements:

(1) A BEMC energy cluster is required to be associated with at least one reconstructed space point in the BPC. The distance between the cluster centre-of-gravity and the BPC space point is required to be smaller than 5 cm (about 3σ of the cluster position resolution).

(2) The lateral size of the cluster is required to be smaller than 5 cm, as expected for the signature of an electron.

(3) Events which have a large fraction of tracks pointing outside the interaction region are rejected.

(4) An event vertex, reconstructed from tracks in the central tracker, within ± 50 cm from the nominal interaction point is required.

(5) The missing energy, $E_{\text{miss}} = E_e \cdot (y_e - y_h)$, is required to be smaller than 11.7 GeV.

Requirements (1) and (2) define the scattered electron candidate. Requirements (3) and (4) reject beam-induced background events while requirement (5) is important for the reduction of radiative corrections and photoproduction background as will be discussed below.

Beam related background can be studied directly with proton and electron pilot bunches. No pilot bunch event survives the final cuts (1)–(5). A detailed study of background events from the pilot bunches over a larger kinematic range and varying cuts gives an upper limit of remaining beam background of at most 1% overall.

The distributions of the basic kinematical variables used in the analysis are shown in figs. 1 and 2 and compared to a Monte Carlo which includes a full simulation of the H1 detector. Note that the Monte Carlo calculations depend on the input structure function.

All Monte Carlo distributions are normalized to the integrated luminosity of our data sample, and are based on the MRSD– parton densities [11]. The energy spectrum of the scattered electron for deep inelastic event candidates is shown in fig. 1a before the cluster size cut (2) and the E_{miss} cut (5). A salient feature of the ep kinematics is a peak of the E'_e distribution near the electron beam energy. Its shape and position are only weakly dependent on the input structure function. The kinematic peak allows to calibrate the E'_e measurement with an accuracy of about 2% which represents an important cross-check of the energy calibration based on the hadron and electron angles. Fig. 1b shows the distribution of the scattering angle θ_e for the events with the cut (2) imposed. The steep rise towards large θ_e reflects the $1/Q^4$ photon propagator effect on the cross section. The y_h distribution is shown in fig. 2a after cuts (1)–(4). The y_e

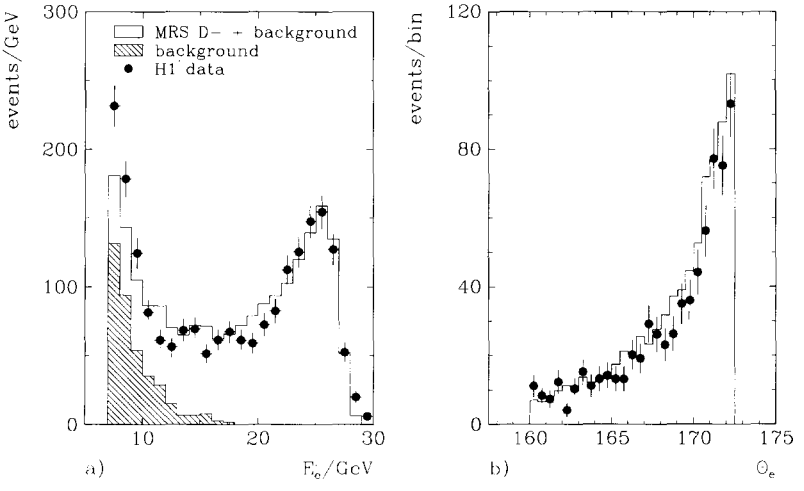

Fig. 1. Distributions of (a) the energy E'_e of the scattered electron before cuts (2) and (5), and (b) the electron scattering angle θ_e in the BEMC angular range imposing cut (2) for $E_e > 10.4$ GeV. The solid histograms are the Monte Carlo predictions normalized to the integrated luminosity of the data sample. The shaded histogram in (a) is the predicted background due to photoproduction events with a fake electron.

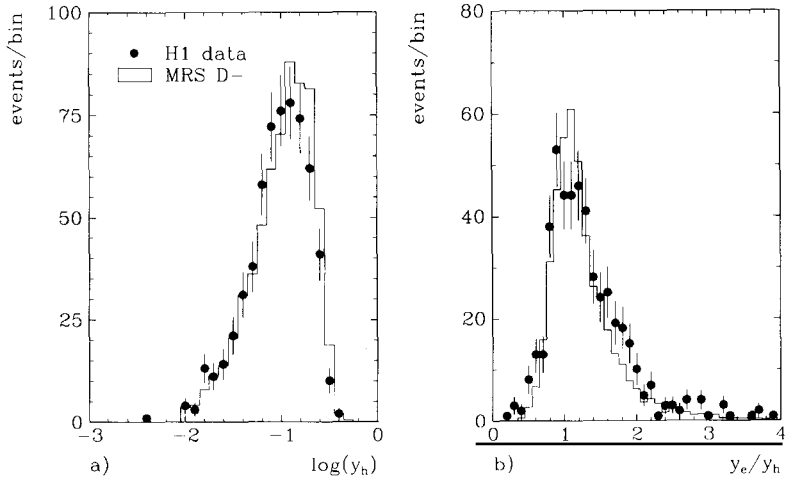

Fig. 2. Distributions of (a) the scaling variable y_h measured with the hadrons for $E_e > 10.4$ GeV, and (b) the ratio y_e/y_h for $0.05 < y < 0.3$. The distributions are obtained after the cuts (1)–(4). The solid histograms are the Monte Carlo predictions normalized to the integrated luminosity of the data sample.

and y_h measurements are compared in fig. 2b which shows the ratio y_h/y_e for $0.05 < y < 0.3$. As expected the distribution peaks at 1. The resolution is well described by the Monte Carlo simulation.

The Monte Carlo events have been generated using HERACLES [12] for the electroweak interaction, which includes first-order radiative corrections, followed by LEPTO [13] for the simulation of QCD processes and fragmentation. The Monte Carlo simulation with the MRSD– parton distributions describes the distributions of figs. 1 and 2 well. It is used in the following for determining the geometrical acceptance and detector smearing corrections.

3.2. PHOTOPRODUCTION BACKGROUND

The most important limitation in extending the measurement domain towards high y ($y > 0.6$) comes from the background of photoproduction processes. These are ep collisions at $Q^2 \sim 0$, which outnumber by several orders of magnitude the deep inelastic collision rate. In these collisions the electron is scattered at small angle and is not observed in the BEMC. However, the hadrons produced in the collision may give rise to a signal in the BEMC, which could be misidentified as that of a deep inelastically scattered electron. The size of this photoproduction background is determined by detailed Monte Carlo simulation studies based on PYTHIA [14] and RAYVDM [15] γ–p event generators, which describe hard and soft processes at $Q^2 \sim 0$, respectively. The overall normalization and the ratio of the hard and soft contributions needed to describe our data have been determined by studying deep inelastic event candidates, surviving cuts (1)–(4), for which an electron is detected in the electron-tagging calorimeter. These events are pure γ–p interactions. Their detection efficiency is $\simeq 10\%$ due to the geometrical acceptance of the tagging calorimeter. The Monte Carlo simulation describes the electron-tagged background sample well in all kinematical variables relevant for this analysis. The relative contributions and the overall normalization are found to be in good agreement with our photoproduction cross section analysis, presented in ref. [16]. This gives us confidence that the Monte Carlo simulation can be applied to the full untagged data sample as well.

The predicted energy spectrum of these γ–p events with fake electron candidates is included in fig. 1a normalized to the total integrated luminosity. It falls rapidly with increasing energy, E'_e, becoming negligible at 16 GeV. In order to reduce this background to a manageable level we require that the cluster energy in the BEMC is larger than 10.4 GeV corresponding to y to be less than 0.6. A significant suppression of the γ–p background is achieved by applying cut (2) and the E_{miss} cut (5). For γ–p events, the scattered electron is missing leading to a large value of E_{miss}. The remaining photoproduction background is found

to be less than 30 % at the highest y (lowest energy E'_e), becoming negligible at $y \leqslant 0.4$. This residual contamination is subtracted statistically.

4. Differential cross section

The differential cross sections are determined by several separate analysis chains, using different combinations of kinematical variables and different unfolding procedures. They are all found to give the same results within errors.

In this paper we present results obtained by two methods which are very different with respect to systematic uncertainties and therefore allow an important cross-check of the final result. In method I, the event kinematics is calculated from the scattered-electron variables E'_e and θ_e according to eqs. (1) and (3). The acceptance, efficiency and cross section are determined in $\sqrt{E'_e}$, θ_e bins which match the resolution and geometrical acceptance of the detector. The calculated cross sections in these detector-oriented bins are then transformed to cross sections in x_e and Q^2_e. In method II, bins in the variables x_m, eq. (5), and Q^2_e are used directly for cross section, acceptance and efficiency calculations. Method I extends the accessible range to large y, method II to low y.

4.1. KINEMATICAL DOMAIN

The kinematical region in which the measurement is made is defined by the following boundaries: $E'_e > 10.4$ GeV and $160.0° < \theta_e < 172.5°$. The angular cuts ensure full containment of the electron shower in the BEMC calorimeter. Method II is restricted to the region $x_m < 0.02$ and $y_h < 0.3$. These limits ensure that a large fraction of the energy of the produced quark jet is contained in the LAr calorimeter.

4.2. EFFICIENCY OF EVENT SELECTION

The efficiencies of the cuts used to select the final data sample are determined directly from the data. The uncertainties in the following efficiencies contribute to the overall normalization error:

–The efficiency of the BEMC electron trigger. The trigger is fully efficient for electrons of energies larger than 10 GeV.

–The TOF-veto requirement. Losses due to false TOF vetoing of genuine deep inelastic events amount to $4 \pm 3\%$.

–Losses of deep inelastic events by cut (4) on the position of the reconstructed vertex amount to $10 \pm 2\%$.

The above contributions, together with a luminosity uncertainty of 7% [16] lead to a global normalization uncertainty of 8%.

The following efficiencies are found to depend on the kinematical variables:

–The efficiency of selecting electron candidates (cut (1) and (2)) amounts to $86 \pm 5\%$ at the highest energies. At the lowest energy it decreases to $77 \pm 7\%$.

–The event-selection efficiency resulting from cut (3) amounts to $92 \pm 3\%$ for events with a reconstructed vertex and varies weakly with the electron energy and angle.

–The efficiency for reconstructing the interaction vertex (cut (4)) is determined to be $93 \pm 6\%$ at lower angles and drops to $79 \pm 6\%$ for the larger angles in the region $E'_e < 25$ GeV .

–The efficiency of cut (5) on E_{miss}. This cut rejects radiative deep inelastic scattering events in which a hard photon is emitted in the direction of the incoming electron, see section 5.

4.3. DETECTOR ACCEPTANCE AND RESOLUTION EFFECTS

Acceptance and smearing corrections are determined from detailed simulation of large event samples. Several different assumptions on input parton densities are used including those predicting a steep rise at low x (MRSD–) as well as those predicting a slow increase (MRSD0).

In method I three equidistant θ_e bins and eight equidistant bins in $\sqrt{E'_e}$, matching the energy dependence of the BEMC resolution, are used. In method II three Q^2 bins and four x bins per decade are chosen. The choice of large bin sizes in both methods is determined by the limited statistics of the data rather than by resolution considerations. As a result smearing corrections are less than 10% everywhere. No significant systematic dependence of the acceptance corrections upon the assumed form of the input parton densities is observed. The residual differences are included in the systematic errors of the data points. The measured differential cross sections are extrapolated to the centre of each bin using the MRSD– parametrization of parton densities. The corrections are below 10% and do not depend significantly on the exact shape of F_2.

5. Radiative corrections

The measured differential cross section, $d^2\sigma^{meas}/dx dQ^2$ contains contributions from higher order electroweak processes, but for $Q^2 \ll M_Z^2$ only electromagnetic radiative processes are relevant. Since the structure functions are defined in the Born approximation, radiative corrections to $d^2\sigma^{meas}/dx dQ^2$ have to be calculated and applied prior to the extraction of F_2. These corrections are traditionally expressed by $\delta(x, Q^2)$ defined by the equation

$$\sigma^{meas}/\sigma^{Born} = (1 + \delta). \tag{6}$$

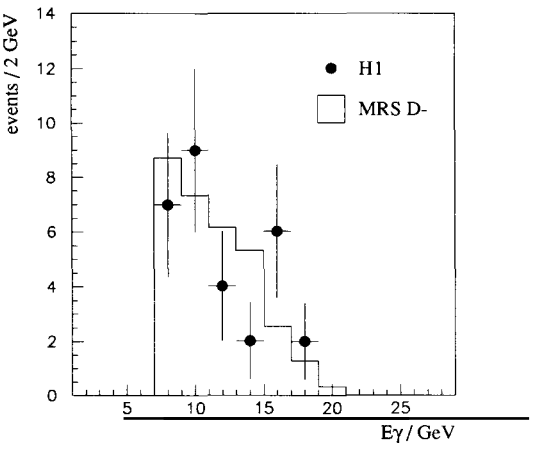

Fig. 3. Distribution of the photon energy E_γ for deep inelastic events with collinear bremsstrahlung as measured in the photon-tagging calorimeter (full points) compared to the Monte Carlo prediction, normalized to the integrated luminosity of the data sample.

Different programs to calculate the radiative corrections are available. We used the numerical program TERAD91 [17] and the Monte Carlo programs HERACLES [12] and LESKO [18] which are found to agree within the statistical accuracy of the Monte Carlo simulation.

The radiative corrections to the cross section measured by the electron variables, $\delta^e(x_e, Q_e^2)$, are sensitive to the shape of the parton distributions in the unaccessible kinematical domain for $Q^2 < 5$ GeV^2 and could exceed 100 % [19]. The corrections are dominated by hard-photon emission in a direction close to that of the incident electron. A fraction of these hard photons can be observed in the photon tagger. In fig. 3 the measured energy distribution of radiative photons with $E_\gamma > 7$ GeV is compared with the prediction of the HERACLES program normalized to the integrated luminosity of our data sample. Good agreement is observed both in shape and magnitude, providing an important check of the theoretical calculation of the corresponding radiative corrections.

The size of the radiative corrections is significantly reduced by the E_{miss} cut which eliminates events with hard initial-state collinear bremsstrahlung with $E_\gamma > 11.7$ GeV. In addition, low hadronic mass Compton events [20] are eliminated by the requirement of a reconstructed vertex. Collinear final-state radiation photons are not resolved in our calorimetric measurement of the scattered electron, leading to a further reduction of the corrections. The radiative corrections of method I are calculated using the event generator HERACLES and its interface to the fragmentation program LEPTO. The resulting radiative corrections for the selected data sample are small (<10%) and almost insensitive to the assumed form of the parton distributions. We have verified, using the LESKO

program, that the contribution of the processes with multiple photon emission to the radiative corrections can be neglected in the measured kinematical domain.

The corrections for the cross section measured in terms of the mixed variables $\delta^{m}(x_m, Q_e^2)$, are calculated using the TERAD91 program and are found to be smaller than 8 %. In method II we have not imposed the E_{miss} cut which would reduce the amount of radiative corrections even further.

6. The structure function $F_2(x, Q^2)$

The Born cross section for deep inelastic electron scattering off a proton can be expressed in terms of the structure function F_2 and the photoabsorbtion cross section ratio of longitudinally and transversely polarised photons, $R = \sigma_L/\sigma_T$:

$$\frac{d^2\sigma}{dx dQ^2} = \frac{2\pi\alpha^2}{Q^4 x}\left(2\,(1-y) + \frac{y^2}{1+R}\right) F_2(x, Q^2), \tag{7}$$

for $Q^2 \ll M_Z^2$. The ratio $R(x, Q^2)$ has not yet been measured at HERA. Therefore, in order to extract $F_2(x, Q^2)$ from the measured differential cross section, an assumption on R has to be made. We have chosen R values calculated according to the QCD prescription [21] using the MRSD– parton distributions. Note that R contributes to the differential cross section mainly in the high-y region. In the region of our measurement the chosen R values reduce the cross section by at most 8% w.r.t. assuming $R = 0$.

The binning for the $F_2(x, Q^2)$ measurement presented in this paper is optimized for studying the x-dependence at fixed values of Q^2. We present the data in four different Q^2 bins, with values of 8.5, 15, 30 and 60 GeV^2. At $Q^2 = 8.5$ GeV^2, only the low-x (large-y) domain is accessible due to the limited angular acceptance of the BEMC. In this region the F_2 measurement comes solely from the electron measurement (method I). At $Q^2 = 60$ GeV^2, the high-x (low-y) domain is measured, where the results based on the mixed (x_m, Q_e^2) variables (method II) are more accurate than the electron measurement. For the two intermediate Q^2 values a meaningful comparison can be made between the two methods.

The rapidly deteriorating resolution in y_e with decreasing y_e, prevents accurate measurements of F_2 at large x with fine binning. Nevertheless, one can assign all events with $y_e < 0.06$ to one single bin, for which efficiencies and acceptances can be determined reliably. Events in this region have x_e values in the range $6 \times 10^{-3} < x_e < 1$, largely overlapping with the existing lower-energy muon proton data. We use the measured shape of F_2 from lower-energy muon proton data to calculate the average x value of this bin. In this way, a point at high x is obtained for the two Q^2 bins at 15 and 30 GeV^2, which links directly to the low-energy data.

The calculation of the systematic errors on F_2 includes the following contributions:

–Possible shifts of the electron energy scale by 2%. This affects mostly method I giving rise to a 20% error at large x, decreasing rapidly towards lower x to 4%. In method II, these errors do not exceed 6%.

–Uncertainty in the BEMC energy resolution of 2%, affecting mostly method I, and yielding errors of up to 6% in the large-x region.

–Uncertainty in the measurement of y_h, affecting method II only. This includes the fragmentation model dependence, an absolute scale uncertainty of the hadronic energy measurement in the LAr calorimeter of 7%, and effects resulting from the treatment of noise in the calorimeter. The corresponding error varies between 10% and 25%. The largest error occurs at low x.

–Possible shifts of θ_e by 5 mrad giving rise to errors of up to 8% for both methods.

– Uncertainty in the event selection efficiency (section 4.2) leading to an error of about 10%.

–Uncertainty in the electron and proton beam induced background (4% for the lowest x value).

–Uncertainty in the photoproduction contamination giving rise to an error of up to 10% for the four lowest-x points.

–Uncertainty in the detector acceptance calculation due to the assumed form of the input parton distributions, giving rise to at most a 10% error.

–Uncertainty in the size of the radiative corrections giving rise to an error of up to 8%, for method I, and up to 3% for method II.

–Uncertainty in the bin centre correction giving rise to errors of up to 5%.

–Global 8% normalization uncertainty as discussed in section 4.2.

The F_2 measurements of method I and II are presented in fig. 4 for two Q^2 values, together with data points from the NMC [22] and BCDMS [23] fixed-target muon proton scattering experiments. The statistical and point-dependent systematic errors are added in quadrature. The global systematic error of 8% is not shown in the figure. The results of method I and of method II, which are to a large extent subject to different systematic effects, are found to be in good agreement. The high-x data points agree well with the available measurements from fixed-target experiments giving us an independent cross-check of the absolute normalization with an accuracy of $\sim$ 20%.

A unique F_2 in the full range of x and Q^2 is obtained by taking the systematically more accurate F_2 values. The final data sample comprises 1026 events. Double counting of events is avoided. Our final results on F_2 are summarized in table 1, together with the R values used in this analysis. The systematic errors for the data points range from 15% to 22%. They include neither the 8% global normalization uncertainty, nor the effect on F_2 due to the uncertainty of R. A substantial reduction of these errors will be possible in the future as more

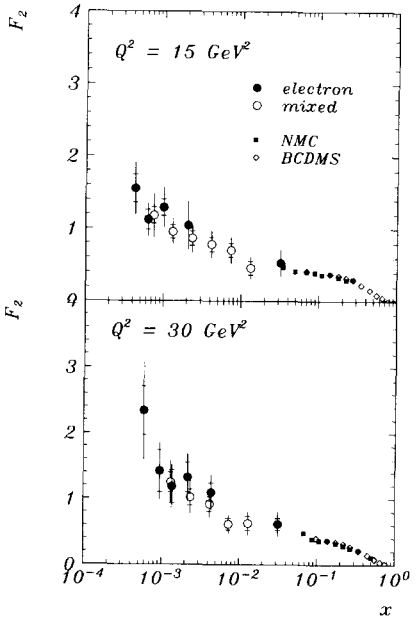

Fig. 4. Measurement of $F_2(x, Q^2)$ for two values of Q^2. The full circles correspond to method I (electron measurement), while the open circles correspond to method II (mixed variable measurement). The error bars show statistical and total errors obtained by adding the statistical and systematic errors in quadrature. In addition all points have a normalization uncertainty of 8%. Data points of the fixed-target muon proton scattering experiments NMC and BCDMS are shown for comparison.

statistics becomes available.

In studying the hadronic final state of the deep inelastic events, we found that the majority of events with the produced quark jet at large angle have a significant energy flow at smaller angles (in the proton direction). This energy flow is described by models which include proton remnant fragmentation, initial state radiation and colour string effects [24]. However, a fraction of events shows no significant energy deposit outside of the produced quark jet region. The same observation has recently been made by the ZEUS collaboration [25]. The maximum pseudorapidity, $\eta = -\ln(\tan\theta/2)$, for energy clusters measured in our calorimeter is 3.8. A class of "rapidity gap" events is defined by asking that no energy cluster with $E_{\text{clust}} > 400$ MeV is found for $\eta > 1.8$. In our deep inelastic sample we find 6% of rapidity gap events while the Monte Carlo calculation [13] predicts only 0.1%. These events are included in the F_2 measurement. A specific study shows that their fraction—within the limited statistics—does not depend significantly on x and Q^2. Thus they play no special role for the rise of F_2 at

TABLE 1

The proton structure function $F_2(x, Q^2)$ as measured in the present experiment. The errors do not include an overall normalization uncertainty of 8%. The statistical (σ_{stat}) and systematic (σ_{syst}) errors are quoted separately. The last column gives the value of $R = \sigma_L/\sigma_T$ used to evaluate F_2. The uncertainty due to R is not included in the errors since F_2 can be reevaluated from this table as soon as better information on R becomes available.

Q^2/GeV^2	x	y	F_2	σ_{stat}	σ_{syst}	R
8.5	0.00018	0.54	1.43 ± 0.52	0.30	0.43	0.42
	0.00024	0.40	1.62 ± 0.39	0.25	0.30	0.39
	0.00032	0.30	1.28 ± 0.27	0.18	0.20	0.36
15	0.00043	0.40	1.56 ± 0.36	0.19	0.30	0.34
	0.00063	0.27	1.13 ± 0.24	0.14	0.19	0.32
	0.00100	0.17	1.30 ± 0.27	0.11	0.25	0.30
	0.00237	0.072	0.87 ± 0.19	0.10	0.16	0.28
	0.00421	0.041	0.78 ± 0.19	0.10	0.16	0.26
	0.00750	0.023	0.71 ± 0.18	0.10	0.15	0.23
	0.01334	0.013	0.46 ± 0.15	0.09	0.12	0.20
30	0.00060	0.57	2.35 ± 0.77	0.37	0.67	0.28
	0.00096	0.35	1.43 ± 0.44	0.32	0.30	0.27
	0.00138	0.25	1.19 ± 0.33	0.25	0.22	0.25
	0.00237	0.14	1.03 ± 0.25	0.12	0.22	0.24
	0.00421	0.081	0.92 ± 0.20	0.11	0.17	0.22
	0.00750	0.046	0.62 ± 0.15	0.09	0.12	0.20
	0.01334	0.026	0.63 ± 0.18	0.11	0.14	0.17
60	0.00237	0.29	1.50 ± 0.52	0.31	0.43	0.21
	0.00421	0.16	0.92 ± 0.28	0.19	0.21	0.20
	0.00750	0.091	1.34 ± 0.36	0.20	0.30	0.18
	0.01334	0.051	0.67 ± 0.21	0.14	0.15	0.15

small x. It will be interesting to study them in detail, since they may be linked to hard diffraction [26] possibly giving information on the pomeron structure function.

7. Discussion

The x-dependence of F_2 is shown in fig. 5 for the four Q^2 values. We observe a clear rise of F_2 with decreasing x. Such a rise is not expected from Regge parton models. On the contrary linear evolution equations in perturbative QCD predict a fast growth of the gluon density in the proton in the asymptotic limit $x \to 0$. An evolution equation derived by Kuraev, Lipatov and Fadin [7], particularly adapted to study the small x region, predicts a characteristic $x^{-\lambda}$ behaviour of the gluon density at small x, with $\lambda \sim 0.5$. Since in this low-x regime the gluon is expected to drive the sea-quark distribution, a similar x-dependence could be

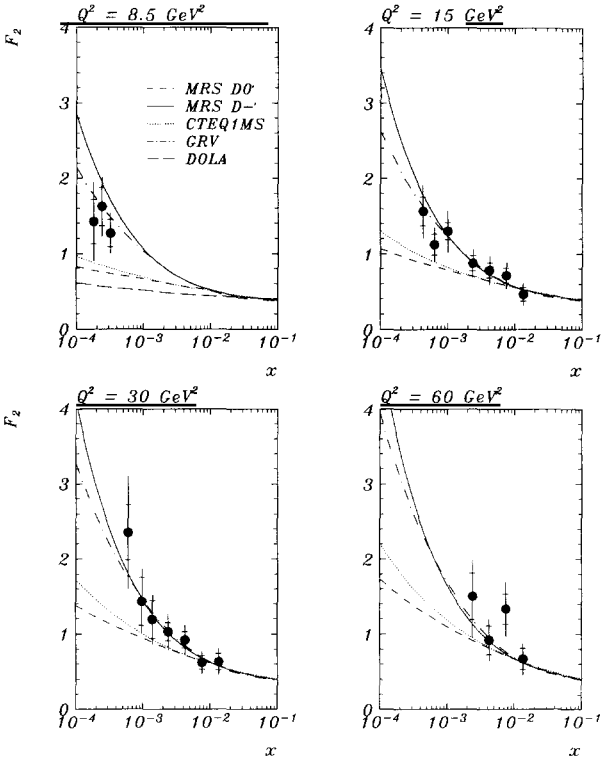

Fig. 5. The measured structure function $F_2(x, Q^2)$ for different values of Q^2, compared to several structure function parametrizations which are fitted to recent low-energy data, described in the text. The error bars show statistical and total errors obtained by adding the statistical and systematic errors in quadrature. In addition all points have a normalization uncertainty of 8%.

expected for F_2. It is however a priori not known at which x value the onset of the Lipatov behaviour should become visible. In any case, it is exciting to see F_2 rise at small x, since interesting QCD effects, such as screening and saturation, may become detectable at HERA. The Q^2 dependence of F_2 is shown in fig. 6 for $Q^2 > 10$ GeV^2. For constant values of x, F_2 increases slowly with Q^2 as could be expected from perturbative QCD.

Various parton density parametrizations exist, which result from fits to mainly low-energy deep inelastic scattering data. Due to the absence of experimental data prior to the HERA results, these parametrizations generally make assumptions on the behaviour of the parton densities at x values below 10^{-2}. Some examples of F_2 structure functions calculated for different parton density parametrizations are shown in figs. 5 and 6. For the MRSD[27] parametriza-

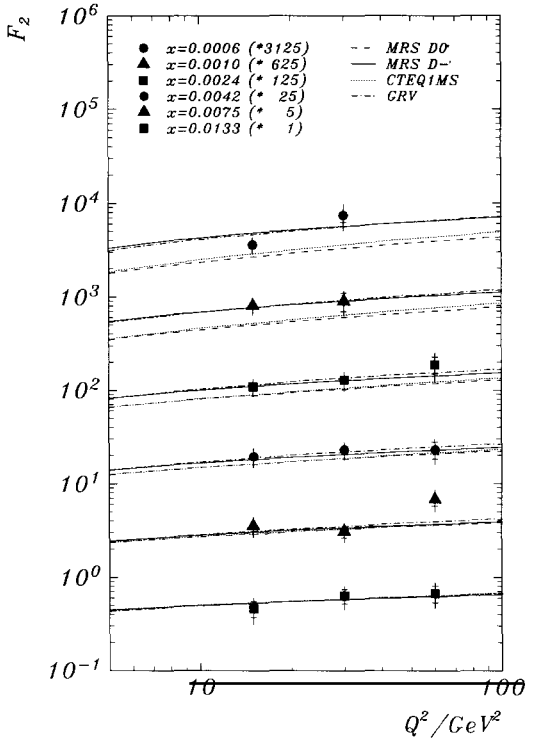

Fig. 6. The measured structure function $F_2(x, Q^2)$ for different values of x, compared to several structure function parametrizations which are fitted to recent low-energy data, described in the text. Notice that the figure does not display the lowest-x data points, table 1, as these are available only at one value of $Q^2 = 8.5$ GeV^2. The error bars show statistical and total errors obtained by adding the statistical and systematic errors in quadrature. In addition all points have a normalization uncertainty of 8%.

tions the small x evolution of the gluon density (at $Q_0^2 = 4$ GeV) is singular (Lipatov behaviour) $\sim x^{-0.5}$ for MRSD−′ and constant for MRSD0′. Similarly, for the CTEQ1MS[28] parametrization the gluon density is singular, but the sea quark distribution is not strongly coupled to the gluon density, leading to a slower rise of F_2 with decreasing x. For the GRV[29] parametrization small x partons are radiatively generated according to the Altarelli–Parisi equations, starting from "valence like" quark and gluon distributions at $Q_0^2 = 0.3$ GeV^2. The parametrization of Donnachie and Landshoff (DOLA) [30] is a Regge-theory motivated fit, which is applicable for Q^2 values up to about 10 GeV^2.

These parametrizations, which all describe the existing low-energy fixed-target data give F_2 values at $x \simeq 10^{-4}$ which differ by more than a factor 4. Our

data are consistent with the GRV and also the MRSD−′ parametrizations. The present measurement narrows the possible range of parton densities at low x substantially, giving a much better basis to predict hard scattering processes at high-energy pp and heavy-ion colliders. Moreover, it gives guidelines for the development of a better theoretical description of the low-x region.

We are grateful to the HERA machine group whose outstanding efforts made this experiment possible. We appreciate the immense effort of the engineers and technicians who constructed and maintain the detector. We thank the funding agencies for financial support. We acknowledge the support of the DESY technical staff. We also wish to thank the DESY directorate for the hospitality extended to the non-DESY members of the collaboration.

References

[1] E.D. Bloom et al., Phys. Rev. Lett. 23 (1969) 930;
M. Breidenbach et al., Phys. Rev. Lett. 23 (1969) 935
[2] F. Brasse, Proc. 26th Int. Conf. on High energy physics, Dallas, ed. J.R. Sanford (1992) p. 1849; DESY preprint 92-140 (1992);
H1 Collab., I. Abt et al., The H1 Detector at HERA, DESY preprint 93-103 (1993)
[3] M. Erdmann et al., New results from the H1 experiment at HERA on photoproduction, deep inelastic scattering and searches for new particles, DESY preprint 93-077 (1993);
A. De Roeck, Deep inelastic scattering at low-x. Results from the H1 experiment, DESY preprint 93-087 (1993)
[4] ZEUS Collab., M. Derrick et al., Measurement of the proton structure function F_2 in ep scattering at HERA, DESY preprint 93-110 (1993)
[5] H1 Collab., T. Ahmed et al., Phys. Lett. B299 (1993) 385
[6] A. Blondel and F. Jacquet, Proc. Study of an *ep* facility for Europe, ed. U. Amaldi, DESY 79-48 (1979) p. 391
[7] E.A. Kuraev, L.N. Lipatov and V.S. Fadin, Phys. Lett. B60 (1975) 50; Zh.E.T.F 72 (1977) 377
[8] L.V. Gribov, E.M. Levin and M.G. Ryskin, Nucl. Phys. B188 (1981) 555; Phys. Rep.100 (1983) 1
[9] H1 Collab. B. Andrieu et al., The H1 liquid argon calorimeter system, DESY preprint 93-078 (1993) to be published in Nucl. Instr. and Meth.
[10] H1 Calorimeter Group, B. Andrieu et al., Results from pion calibration runs for the H1 liquid argon calorimeter and comparisons with simulations, DESY preprint 93-047 (1993), to be published in Nucl. Instr. and Meth.
[11] A.D. Martin, W.J. Stirling and R.G. Roberts, Phys. Rev. D47 (1993) 867
[12] A. Kwiatkowski, H. Spiesberger and H.-J. Möhring, Comput. Phys. Commun. 69 (1992) 155 and references therein
[13] G. Ingelman, LEPTO 5.2, unpublished program manual;
H. Bengtsson, G. Ingelman and T. Sjöstrand, Nucl. Phys. B301 (1988) 554;
G.A. Schuler and H. Spiesberger, Proc. Workshop Physics at HERA, ed. W. Buchmüller and G. Ingelman, Hamburg (1991) p. 1419
[14] H. Bengtsson and T. Sjöstrand, Comput. Phys. Commun. 46 (1987) 43;
T. Sjöstrand, CERN-TH-6488-92 (1992)
[15] N.H. Brook, A. De Roeck and A.T. Doyle, RAYPHOTON 2.0, Proc. Workshop Physics at HERA, ed. W. Buchmüller and G. Ingelman, Hamburg (1991) p. 1453
[16] H1 Collab., T. Ahmed et al., Phys. Lett. B299 (1993) 374

[17] A. Akhundov et al., Proc. Workshop Physics at HERA, ed. W. Buchmüller and G. Ingelman, Hamburg (1991) p. 1285
[18] W. Placzek, Proc. Workshop Physics at HERA, ed. W. Buchmüller and G. Ingelman, Hamburg (1991) p. 1433
[19] M. W. Krasny, Proc. Workshop Physics at HERA, ed. W. Buchmüller and G. Ingelman, Hamburg (1991) p. 850
[20] A. Courau et al. Proc. Workshop Physics at HERA, ed. W. Buchmüller and G. Ingelman, Hamburg (1991) p. 902
[21] G. Altarelli, G. Martinelli, Phys. Lett. B76 (1978) 89
[22] NMC Collab., P. Amaudruz et al., Phys. Lett. B295 (1992) 159; Erratum to CERN-PPE/92-124, CERN (April 1993)
[23] BCDMS Collab., A.C. Benvenuti et al., Phys. Lett. B223 (1989) 485
[24] H1 Collab., T. Ahmed et al., Phys. Lett. B298 (1993) 469
[25] ZEUS Collab., M. Derrick et al., Observation of events with a large rapidity gap in deep inelastic scattering at HERA, DESY preprint 93-093 (1993)
[26] G. Ingelman and P.E. Schlein, Phys. Lett. B152 (1985) 256;
A. Donnachie and P.V. Landshoff, Phys. Lett. B191 (1987) 309;
M. G. Ryskin, Sov. J. Nucl. Phys. 53 (1991) 668
[27] A.D. Martin, W.J. Stirling and R.G. Roberts, Phys. Lett. B306 (1993) 145; B309 (1993) 492
[28] J. Botts et al., Phys. Lett. B304 (1993) 159
[29] M. Glück, E. Reya and A. Vogt, Z. Phys. C53 (1992) 127; Phys. Lett. B306 (1993) 391
[30] A. Donnachie and P. V. Landshoff, M/C-th 93/11, DAMTP 93-23